SCIENTIFIC REPORTS
nature research

OPEN

Asymmetric supercapacitor of functionalised electrospun carbon fibers/poly(3,4-ethylenedioxythiophene)/ manganese oxide//activated carbon with superior electrochemical performance

Muhammad Amirul Aizat Mohd Abdah[1], Nur Hawa Nabilah Azman[1], Shalini Kulandaivalu[1] & Yusran Sulaiman[1,2*]

Asymmetric supercapacitors (ASC) have shown a great potential candidate for high-performance supercapacitor due to their wide operating potential which can remarkably enhance the capacitive behaviour. In present work, a novel positive electrode derived from functionalised carbon nanofibers/ poly(3,4-ethylenedioxythiophene)/manganese oxide (*f*-CNFs/PEDOT/MnO_2) was prepared using a multi-step route and activated carbon (AC) was fabricated as a negative electrode for ASC. A uniform distribution of PEDOT and MnO_2 on *f*-CNFs as well as porous granular of AC are well-observed in FESEM. The assembled *f*-CNFs/PEDOT/MnO_2//AC with an operating potential of 1.6 V can achieve a maximum specific capacitance of 537 F/g at a scan rate of 5 mV/s and good cycling stability (81.06% after cycling 8000 times). Furthermore, the as-prepared ASC exhibited reasonably high specific energy of 49.4 Wh/ kg and low charge transfer resistance (R_{ct}) of 2.27 Ω, thus, confirming *f*-CNFs/PEDOT/MnO_2//AC as a promising electrode material for the future energy storage system.

The gradual depletion of fossil fuels and the demand of energy consumption have shown a tremendous effort in developing alternative energy storage devices such as fuel cells, lithium-ion batteries (LIBs), conventional capacitors and supercapacitors has been devoted to overcoming these energy crises. Among them, supercapacitors, also known as electrochemical capacitors or ultracapacitors have outperformed other energy storage devices by virtue of their superior electrochemical characteristics; high specific power, rapid charging/discharging rate and excellent long-term cycling stability[1]. Supercapacitors fill the gap between batteries and normal capacitors, which make them an important device for wide practical applications (hybrid vehicles, portable electronic devices and large-scale production)[2].

Depending on the basis of the charge storage mechanism, supercapacitors are classified into two classes which are electrochemical double layer capacitors (EDLCs) and pseudocapacitors. In EDLCs, the electrical charges are stored via non-faradaic reaction at the electrolyte/electrode interface, while pseudocapacitors store charges by means of reversible redox reactions at the surface of the electrode. Carbon materials such as graphene[3], graphene oxide (GO)[4], carbon nanotubes (CNTs)[5], carbon nanofibers (CNFs)[6] and activated carbon (AC)[7] are the common electrode materials for EDLC, and likewise, conducting polymers (CPs), transition metal oxides (TMOs), transition metal sulfides (TMSs), and transition metal nitrides (TMNs) are utilised as electrodes in pseudocapacitors.

[1]Department of Chemistry, Faculty of Science, Universiti Putra Malaysia, 43400 UPM, Serdang, Selangor, Malaysia. [2]Functional Devices Laboratory, Institute of Advanced Technology, Universiti Putra Malaysia, 43400 UPM, Serdang, Selangor, Malaysia. *email: yusran@upm.edu.my

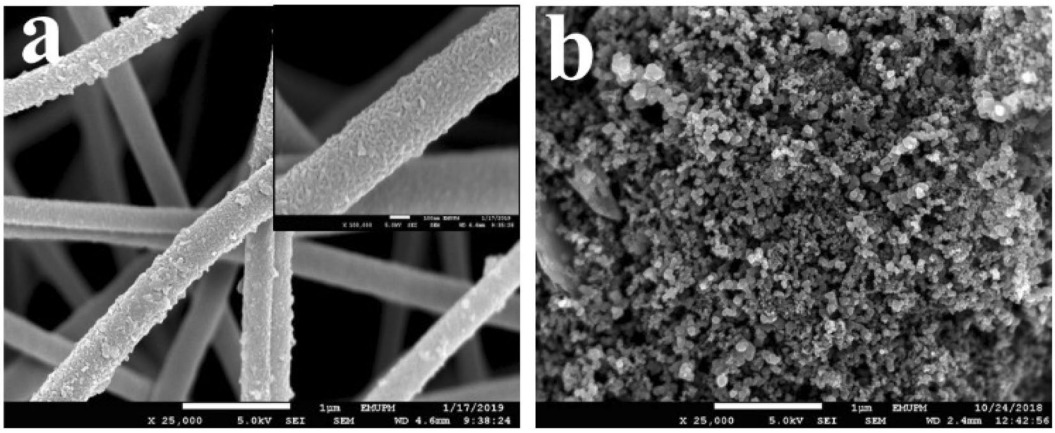

Figure 1. FESEM images of (**a**) *f*-CNFs/PEDOT/MnO_2 (inset: the high-magnification of *f*-CNFs/PEDOT/MnO_2) and (**b**) AC.

Among all carbon materials, CNFs have shown greater potential owing to their large specific surface area, excellent electrical conductivity, good mechanical stability, availability as well as environmental friendly[8]. The tunable diameter and pore size of CNFs can be achieved through a facile and practical combination of electrospinning and carbonisation[9]. However, the individual CNFs suffer from poor specific capacitance and specific energy. CPs including polyaniline (PANi)[10], polypyrrole (PPy)[11–13] and poly(3,4-ethylenedioxythiophene) (PEDOT)[14,15] have drawn extensive interest in supercapacitors, but PEDOT has turned out to be the promising CP due to its excellent intrinsic conductivity and fast electrochemical kinetics[16].

Manganese oxide (MnO_2) is identified as an ideal pseudocapative-material in supercapacitors as it possesses theoretically high specific capacitance (C_{sp}) (1370 F/g), wide operating potential, abundance in nature and non-toxicity characteristics[17]. Despite these advantages, challenges related to poor stability of PEDOT and low specific capacitance of MnO_2 could hinder their practical supercapacitor application in the future. To overcome these problems, extensive efforts have been made in developing hybrid/asymmetric electrodes which combine the advantages of EDLCs and pseudocapacitors to further improve its capacitive performance. Moreover, the surface of CNFs can be altered by adding oxygen-containing functional groups (–COOH, –OH, and C=O), enhancing its surface wettability[18] with better adhesion between active materials and CNFs[19].

Recently, carbon-MnO_x composite fibers have been prepared by Pech and Maensiri[20] using core-shell electrospinning and exhibited high C_{sp} of 213.7 F/g and good cycle durability (∼97%) over 1000 cycles. Śliwak and Gryglewicz[21] reported a facile approach to synthesis MnO_2/oxidised carbon nanofibers (MnO_2/CNFox) and AC as positive and negative electrodes, respectively for asymmetric supercapacitor (ASC). The assembled ASC device with an extended potential window of 2.4 V possessed a remarkable specific energy of 24.8 Wh/kg (specific power at 100 W/kg) as well as excellent capacitance retention of 92.4% after 5000 cycles. Garcia-Torres and Crean[22] reported the preparation of CB/CNT/MnO_2/PEDOT:PSS composite fibers via wet spinning followed by chemical reduction using potassium permanganate ($KMnO_4$) as reducing agent and displayed high C_{sp} of 351 F/g.

In this work, we reported the ASC design of functionalised-CNFs/PEDOT/MnO_2 (*f*-CNFs/PEDOT/MnO_2) composite and AC as positive and negative electrodes, respectively. The *f*-CNFs/PEDOT/MnO_2 was fabricated through several steps; electrospinning, carbonisation, electrochemical functionalisation and electrodeposition of PEDOT and MnO_2. The electrochemical performance was tested individually using three electrode configurations to determine the maximum operating potential achieved by each electrode. The asymmetric device was then assembled with a separator containing 1 M potassium chloride (KCl) electrolyte, and all electrochemical measurements were performed systematically. The synergistic effect contributed from both double layer capacitance and pseudocapacitance of *f*-CNFs/PEDOT/MnO_2//AC has greatly improved its electrochemical performances including specific capacitance, specific energy and cycling stability.

Results and Discussion

Morphology characterisation. The surface morphology of the *f*-CNFs/PEDOT/MnO_2 and AC electrodes were investigated through FESEM as shown in Fig. 1. In Fig. 1(a), the cross-linking structures of the as-prepared fibers are randomly oriented with smooth surface and beads-free. After the inclusion of PEDOT and MnO_2 using the electrochemical approach, uniform growth of PEDOT and MnO_2 nanoparticles on the *f*-CNFs surface can be observed without any aggregation. The presence of abundance oxygenated functional groups attached on CNFs can serve as nucleation sites for the growth of PEDOT and MnO_2[23] and providing better ions diffusion process from the electrolyte onto the electrode[11]. The *f*-CNFs/PEDOT/MnO_2 has an average diameter of 390 ± 68 nm, which is slightly higher as compared with pure *f*-CNFs (354 ± 45 nm)[11]. The high-magnification FESEM image (inset of Fig. 1a) also proves that the coatings of PEDOT and MnO_2 are relatively uniform on the fibrous networks. In Fig. 1(b), the AC electrode displays a homogenous and irregular carbon spheres morphology with an average diameter of 65 ± 12 nm. The void spaces between the AC particles provide more accessible surface sites that allow more contact surface between electrode and electrolyte ions[24]. Therefore, the unique morphology for both positive and negative electrodes can provide good charge propagation behaviour in ASC.

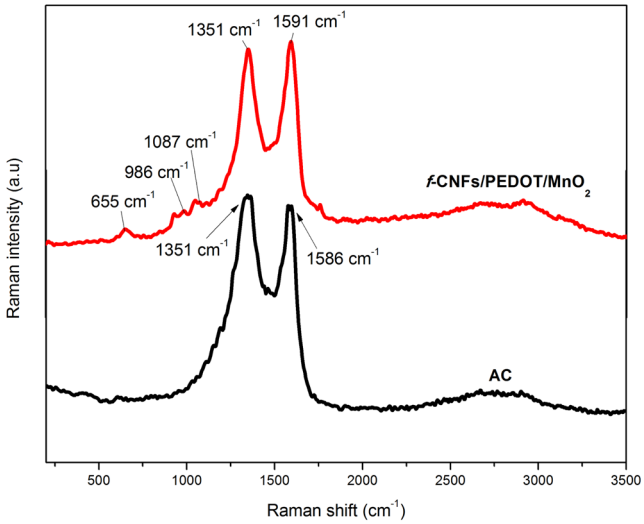

Figure 2. Raman spectra of as-prepared *f*-CNFs/PEDOT/MnO_2 and AC.

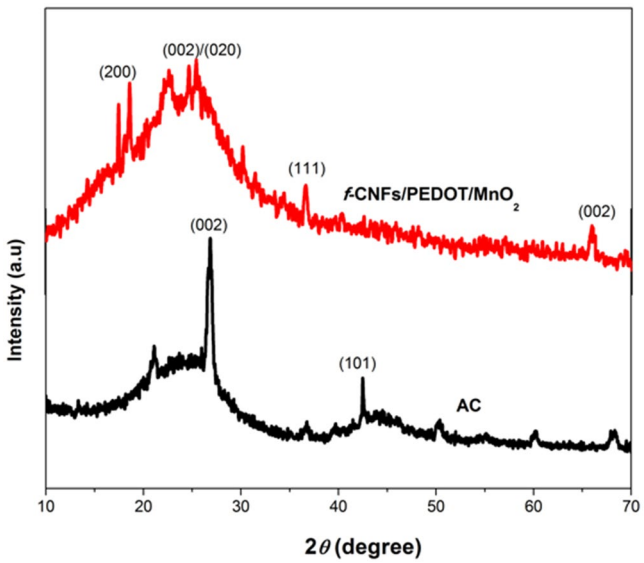

Figure 3. XRD diffractograms of *f*-CNFs/PEDOT/MnO_2 and AC.

Raman spectroscopy. Raman spectroscopy was used to study the functional groups that exist in both *f*-CNFs/PEDOT/MnO_2 and AC electrodes as shown in Fig. 2. Two prominent peaks centred around 1351 and 1586 cm^{-1} in the AC spectrum, corresponding to the D and G bands, respectively. D band is related to the defect/disordered carbon structure (sp^3) while G band originates from the crystalline graphitic layer (sp^2). The D band (1351 cm^{-1}) and G band (1591 cm^{-1}) of the *f*-CNFs are also observed in the Raman spectrum of *f*-CNFs/PEDOT/MnO_2. The presence of PEDOT in the spectrum is confirmed by three vibrational peaks; 986, 1087 and 1351 cm^{-1} which are associated with oxyethylene ring deformation, C–O–C deformation and C–C stretching vibration of PEDOT[25], respectively. The intensity ratio (I_D/I_G) of *f*-CNFs/PEDOT/MnO_2 is 0.85, which is slightly lower compared with AC (0.87), revealing a small number of defects in the sample[26]. In addition, a characteristic peak at 655 cm^{-1} is assigned to the stretching vibration of birnessite-type MnO_2[27].

X-ray diffraction (XRD). The crystallinity of *f*-CNFs/PEDOT/MnO_2 and AC was investigated by XRD analysis, and the corresponding patterns are shown in Fig. 3. In the XRD pattern of *f*-CNFs/PEDOT/MnO_2, a broad peak at $2\theta = 25°$ can be indexed to the (002) diffraction plane of *f*-CNFs[28] with an amorphous or low crystallinity carbon phase[29]. The presence of MnO_2 nanoparticles was confirmed by two diffraction peaks positioned at 37° and 65° which can be identified as the (111) and (002) crystal planes of MnO_2 (JCPDS Card. No. 24-0735)[30]. In addition, the sharp diffraction peaks at $2\theta = 17°$ and 18° corresponded to the (200) plane of tetragonal α-MnO_2 phase (JCPDS 072-1982). Furthermore, a low-intensity peak ($2\theta = 24°$) which is overlapped with the broad peak of *f*-CNFs corresponding to the diffraction peak of PEDOT (020) with high-crystallinity feature[31]. As shown in

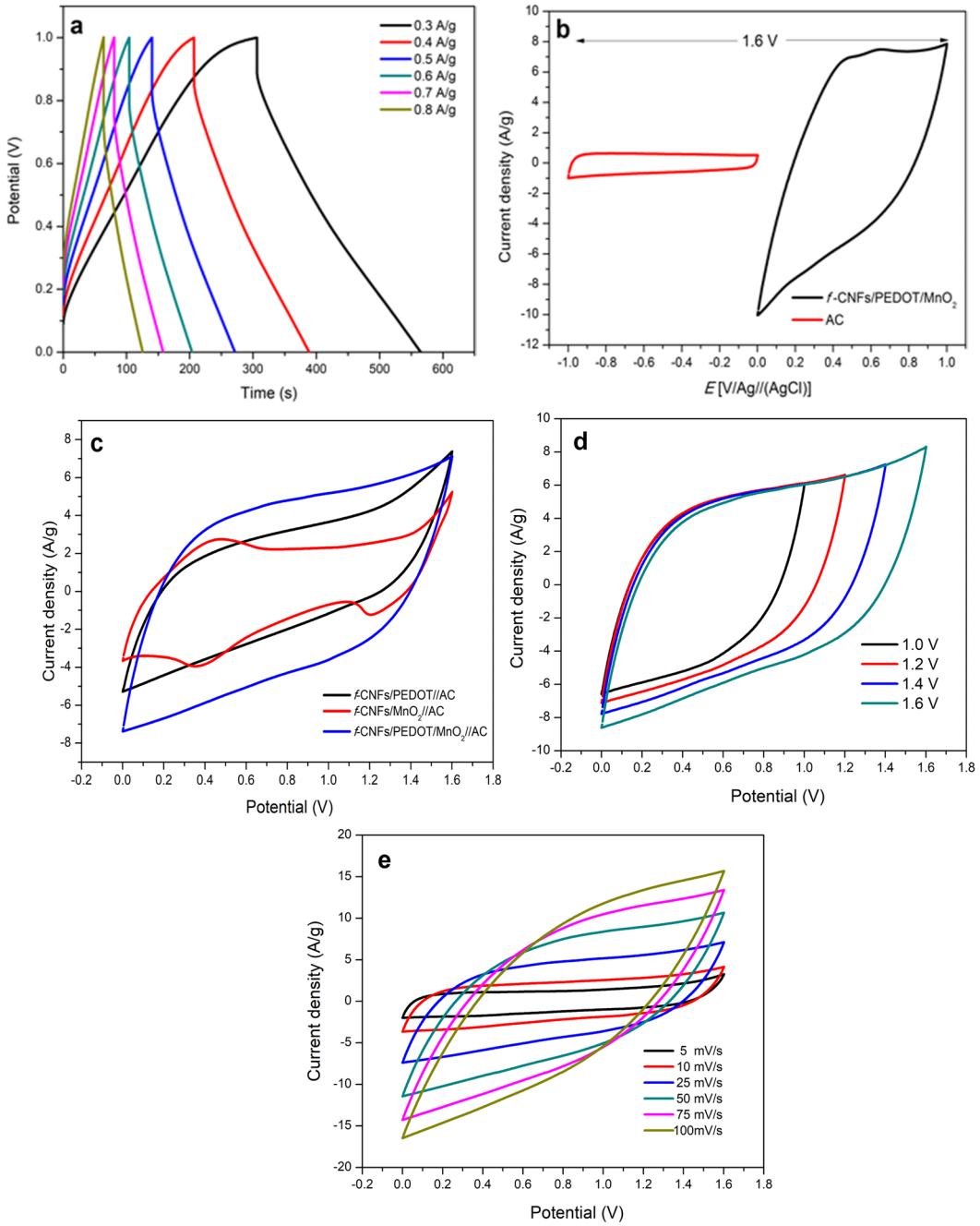

Figure 4. (**a**) GCD curves of *f*-CNFs/PEDOT/MnO_2 at different current densities (0.3–0.8 A/g). (**b**) CV curves of *f*-CNFs/PEDOT/MnO_2 and AC half cells at a scan rate of 25 mV/s. (**c**) CV curves of different asymmetric supercapacitors at a scan rate of 25 mV/s. (**d**) CV curves of asymmetric *f*-CNFs/PEDOT/MnO_2//AC at different potential windows (1.0–1.6 V) using a scan rate of 25 mV/s. (**e**) CV curves of asymmetric *f*-CNFs/PEDOT/MnO_2//AC at different scan rates from 5 to 100 mV/s in 1.0 M KCl electrolyte.

Fig. 3, the typical characteristic of AC is visible at $2\theta = 26°$ (002) and 43.5° (101)[32] with a high degree of graphitic crystallinity. Notably, the additional peaks ($2\theta = 51°$ and 60°) appeared in the AC spectrum can be attributed to the bare ITO glass[33].

Electrochemical measurements. Figure 4(a) displays the charge-discharge behavior of *f*-CNFs/PEDOT/MnO_2 at different current densities to understand its capacitive performance. The GCD curves exhibit nearly symmetrical triangular shape with a small deviation, which could be raised from the pseudo-faradaic reactions of PEDOT and MnO_2 during the charging-discharging process. A noticeable *IR* drop at the initial portion of the discharge curves indicates the small internal resistance of the system at high charge-discharge current densities[34]. To evaluate the electrochemical performance of both *f*-CNFs/PEDOT/MnO_2 and AC electrodes, CV measurements

were carried out in a standard three-electrode setup using 1 M KCl as the electrolyte as shown in Fig. 4(b). The *f*-CNFs/PEDOT/MnO_2 electrode was measured in the potential window of 0 to 1 V (vs. Ag/AgCl) and displays a quasi-rectangular shape, indicating the combination of both EDLC and pseudocapacitance behaviour[35]. However, a small hump observed at 0.56 V is attributed to the redox reaction of the oxygenated functional groups at the surface of the electrode[36] and pseudocapacitance of PEDOT and MnO_2. The *f*-CNFs/PEDOT/MnO_2 electrode exhibits a larger enclosed CV area compared with AC, demonstrating higher charge capacity[37] and higher specific capacitance[38]. For AC, the electrode contributes the potential window from −0.6 to 0 V (vs. Ag/AgCl) with symmetrical rectangular CV curve, indicating an ideal EDLC feature[39] with good rate capability[21]. The C_{sp} for *f*-CNFs/PEDOT/MnO_2 (442.50 F/g) and AC (58.89 F/g) are calculated based on Eq. (1):

$$C_{sp} = \frac{1}{2m \times v \times \Delta V} \int I \, \mathrm{dV} \tag{1}$$

where C_{sp} (F/g) represents specific capacitance, I dV is the integrated area CV curve, v (Vs^{-1}) is the potential scan rates, m (g) is the mass of sample, and dV (V) is the p, ΔV (V) is the potential window (CV) or potential drop during the discharging time (GCD) and I (A) is the applied current. The maximum potential window of the *f*-CNFs/PEDOT/MnO_2//AC can be extended up to 1.6 V. Therefore, the charge of both electrodes need to be balanced in order to obtain a stable asymmetric supercapacitor via Eq. (2):

$$\frac{m_+}{m_-} = \frac{C_- \times \Delta E_-}{C_+ \times \Delta E_+} \tag{2}$$

where m is the mass of electrode, C is C_{sp} of the respective electrode and ΔE is the operating voltage (0.6 V for negative and 1.0 V for positive electrode). The subscript of "+" and "−" relate to positive and negative electrodes. Figure 4(c) displays the CV curves of assembled *f*-CNFs/PEDOT//AC, *f*-CNFs/MnO_2//AC and *f*-CNFs/PEDOT/MnO_2//AC in the potential range of 0 to 1.6 V at a scan rate of 25 mV/s. It can be seen that *f*-CNFs/PEDOT/MnO_2//AC shows a larger area of CV curve among other samples, suggesting high specific capacitance. Impressively, the assembled *f*-CNFs/PEDOT/MnO_2//AC delivers the highest specific capacitance of 354 F/g compared with *f*-CNFs/PEDOT//AC (206 F/g) and *f*-CNFs /MnO_2//AC (155 F/g). The CV curves of assembled *f*-CNFs/PEDOT/MnO_2//AC asymmetric cell at different potential windows (1.0–1.6 V) are shown in Fig. 4(d). It can be seen that the ASC can work stably even at 1.6 V potential window and the quasi-rectangular of CV curves are retained, corresponding to good supercapacitive behaviour. Moreover, the specific capacitance increases from 287 F/g to 354 F/g over extended potential windows, which significantly improve the charge storage capacity of the composite[40].

Figure 4(e) represents the CV of as-obtained ASC at different scan rates, ranging from 5 to 100 mV/s. At lower scan rates, the CV profiles exhibit rectangular-like shape and as the scan rate increases from 50 to 100 mV/s, the CV curves show some distortions from an ideal rectangular shape. This is due to the limitation of the electrolyte ions to diffuse into the active material and only capable to access at the outer surface of the material, leading to the decrease of specific capacitance[41]. The calculated specific capacitance of ASC can achieve 537, 459, 354, 269, 221 and 188 F/g at a scan rate of 5, 10, 25, 50, 75 and 100 mV/s, respectively. The prominent specific capacitance of ASC could be ascribed from the synergistic effect between *f*-CNFs/PEDOT/MnO_2 and AC, where EDLC of *f*-CNFs and AC contribute to a larger ion-accessible surface area, while PEDOT and MnO_2 possess excellent electrical conductivity and high specific capacitance, respectively.

To further examine the electrochemical performance of ASCs, the GCD tests were carried out at a current density of 0.5 A/g as shown in Fig. 5(a). It can be clearly seen that *f*-CNFs/PEDOT/MnO_2//AC electrode exhibits the largest charging-discharging time span, contributing to an excellent capacitive behaviour[42]. GCD measurement was also performed at various current densities; 0.3 to 8 A/g as presented in Fig. 5(b). Apparently, all GCD curves show a nearly triangular shape with a little deviation, corresponding to the signature of a redox-type storage mechanism[43] with good electrochemical reversibility[24]. The specific capacitance of 148.07 F/g is obtained at a current density of 0.3 A/g. Figure 5(c) illustrates the Ragone plot (specific energy *vs* specific power) of *f*-CNFs/PEDOT/MnO_2//AC asymmetric cell which exhibits maximum specific energy of 49.4 Wh/kg with a specific power of 224.02 W/kg at a current density of 0.3 A/g. Furthermore, the specific energy obtained is superior as compared to the reported values for PEDOT- and MnO_2-based fibers for supercapacitor[4,21,39,44–46].

The electrochemical properties of different asymmetric supercapacitors were further analysed using EIS measurements and their Nyquist plots are shown in Fig. 5(d). The plot consists of two regions: high and low frequency regions. At high frequency, the semicircle arc and the intercept of the real axis (Z') indicate the charge transfer resistance (R_{ct}) and equivalent series resistance (ESR), respectively. The straight line in the low-frequency region represents the Warburg impedance (W) for ion diffusion at the electrolyte/electrode interface. The R_{ct} of as-prepared *f*-CNFs/PEDOT/MnO_2//AC, CNFs/PEDOT//AC and *f*-CNFs/MnO_2//AC are 2.27, 1.2 and 2.74 Ω, respectively. A slightly higher R_{ct} of *f*-CNFs/PEDOT/MnO_2//AC in comparison to *f*-CNFs/PEDOT//AC can be ascribed to the low conductivity of MnO_2. Furthermore, the *f*-CNFs/PEDOT/MnO_2//AC electrode shows the lowest ESR value of 35.58 Ω compared to *f*-CNFs/PEDOT//AC (35.63 Ω) and *f*-CNFs/MnO_2//AC (41.28 Ω) as the ESR is attributed to the ionic resistance of the electrolyte, the resistance of the active material and contact resistance between the current collector and active material[47]. The nearly vertical line (close to 90°) at low frequency region of the *f*-CNFs/PEDOT/MnO_2//AC indicates a characteristic of an ideal capacitive behaviour[48]. In addition, *f*-CNFs/PEDOT/MnO_2//AC exhibits the shortest vertical line along the imaginary axis, implying rapid ion diffusion.

The cycling stability test of *f*-CNFs/PEDOT/MnO_2//AC asymmetric cell was performed over 8000 CV cycles at a potential window of 1.6 V (Fig. 5(e)). Remarkably, the ASC device displays good cycling stability and retained

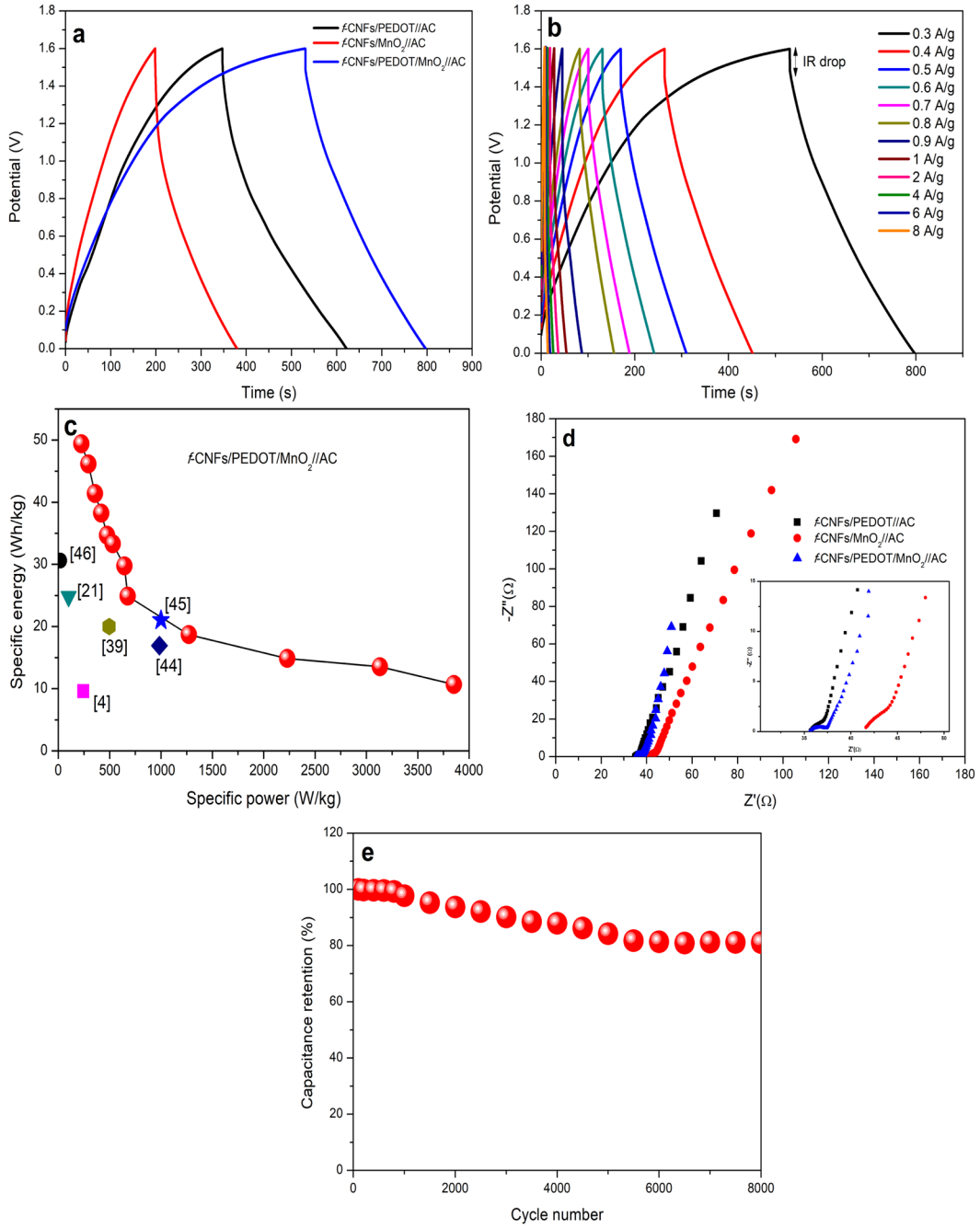

Figure 5. (**a**) GCD curves of different asymmetric supercapacitors at a current density of 0.5 A/g (**b**) GCD curves of asymmetric *f*-CNFs/PEDOT/MnO_2//AC at various current densities (0.3–8 A/g). (**c**) Ragone plot of asymmetric *f*-CNFs/PEDOT/MnO_2//AC. (**d**) Nyquist plot of different asymmetric supercapacitors with a frequency range of 0.01 Hz to 100 kHz. (**e**) The cyclic performance over 8000 cycles of asymmetric *f*-CNFs/PEDOT/MnO_2 //AC electrode at a scan rate of 150 mV/s.

81.06% of its original capacitance after 8000 cycles. A good long-term cycling stability of ASC is mainly contributed from the superior mechanical strength of the *f*-CNFs and AC which effectively can enhance the cyclability during the charging/discharging process.

Conclusions

In summary, a promising positive electrode derived from *f*-CNFs/PEDOT/MnO_2 was successfully fabricated for asymmetric supercapacitor. By combining with AC as a negative electrode, the ASC device induces a strong synergistic effect which greatly enhanced its electrochemical performance. A well-adhered of PEDOT and MnO_2 on the surface of the *f*-CNFs as well the highly porous morphology of AC was beneficial in providing ease ion-diffusion pathways at the electrolyte/electrode interface, thus can increase the specific capacitance. The

assembled *f*-CNFs/PEDOT/MnO//AC could operate reversibly at a maximum voltage of 1.6 V, and displayed specific capacitance as high as 537 F/g, with good cycling stability (81.06%) after 8000 cycles. It also offers high specific energy of 49.4 Wh/kg at a specific power of 224.02 W/kg and low R_{ct}, implying its good rate performance and enhanced conductivity. These outstanding results prove that *f*-CNFs/PEDOT/MnO//AC ASC can hold great potential for achieving high-performance supercapacitors.

Experimental Section

Materials. Indium tin oxide glasses (ITO, 7 Ω/sq) were obtained from Xin Yan Technology Limited. N, N-dimethylformamide (DMF) were supplied by Merck. AC, mesoporous carbon, polytetrafluoroethylene (PTFE), polyacrylonitrile (PAN, Mw = 150,000), silver wire (Ag, diam. 0.5 mm), 3, 4-ethylenedioxythiophene (EDOT, 97% purity), lithium perchlorate ($LiClO_4$, ≥97% purity) and manganese (II) sulfate monohydrate ($MnSO_4 \bullet H_2O$) were purchased from Sigma-Aldrich. KCl and sulphuric acid (H_2SO_4) were acquired from Fisher Scientific. Acetone and ethanol were supplied from HmbG Chemicals and J. Kollin Chemicals, respectively. Deionised water (18.2 MΩ.cm) was used throughout the experiments. All chemicals were directly used as obtained without further purification.

Preparation of *f*-CNFs/PEDOT/MnO_2 (positive) and AC (negative) electrodes. The synthesis of *f*-CNFs/PEDOT/MnO_2 composite was carried out using several steps: electrospinning, carbonisation, electrochemical functionalisation, electropolymerisation and electrodepositon sequentially. In a typical procedure, 10 wt% PAN solution in DMF under continuous stirring and a homogenous precursor solution was loaded into 5 mL syringe and ejected through a 15-gauge stainless steel needle by applying a voltage of 15 kV between needle and collector. The rotating collector covered by aluminium foil was placed 15 cm away from the tip of the needle with a flow rate of 1.0 mL/h and a rotating speed of 200 rpm. The electrospun PAN fibers were then oxidatively stabilised in a mild temperature of 280 °C under an air atmosphere at a heating rate of 1 °C/min. The stabilised fibers were then undergone carbonisation with a heating rate of 5 °C/min up to 800 °C for 2 h under nitrogen (N_2) atmosphere. The attachment of oxygenated functional groups (–COOH, –OH, and C=O) on the CNFs surface was performed in 1.0 M H_2SO_4 via cyclic voltammetry for 2 h to obtain *f*-CNFs. The PEDOT film was electrochemically polymerised on *f*-CNFs at a constant potential of 1.1 V for 15 min, where Ag/Ag^+ and Pt wire were served as a reference electrode and the auxiliary electrode, respectively. The electropolymerisation of EDOT was carried out in a non-aqueous solution consisting of 0.01 M EDOT and 0.1 M $LiClO_4$ in acetonitrile. The MnO_2 nanoparticles (0.05 M $MnSO_4 \bullet H_2O$ solution) was then electrodeposited using cyclic voltammetry with a potential range between 0.1 and 1.0 V for 20 cycles, producing *f*-CNFs/PEDOT/MnO_2 composite. Both electropolymerisation and electrodeposition were performed in a three-electrode configuration using a computer-controlled Autolab 101 potentiostat equipped with Nova 1.10 software. The AC electrode was prepared from an 80:10:10 (wt%) mixture of AC, mesoporous carbon and PTFE, where a few drops of ethanol were added into the mixture to form a slurry. The slurry was pasted onto ITO glass via and further dried in an oven at 50 °C. The mass loading of both *f*-CNFs/PEDOT/MnO_2 and AC electrodes were about 0.5 mg/cm^2 and 0.9 mg/cm^2, respectively.

Characterisations. The morphologies of *f*-CNFs/PEDOT/MnO_2 and AC were examined using field emission scanning electron microscopy (FESEM, JEOL JSM-7600F). The structure and elemental composition of both positive and negative electrodes were identified using Raman spectroscopy (Alpha 300R, 532 nm Ar-ion laser) and X-ray diffraction (XRD, Shimadzu with Cu K$\propto$ radiation ($\lambda = 1.54$ Å)

Electrochemical test. Electrochemical measurements of the individual *f*-CNFs/PEDOT/MnO_2 (positive) and AC (negative) were performed in a three-electrode configuration in 1.0 M KCl electrolyte. An Ag/AgCl and Pt wire were employed as a reference electrode and the auxiliary electrode, respectively. The CV of positive and negative electrodes was recorded at the voltage of 0–1.0 V and −0.6 to 0 V, respectively at a scan rate of 25 mV/s, respectively. The ASC two-electrode configuration was assembled by sandwiching both positive and negative electrodes together with a filter paper soaked in 1.0 M KCl as a separator. A series of electrochemical measurements, including CV, galvanostatic charge-discharge (GCD) and electrochemical impedance spectroscopy (EIS) was performed for ASCs. The CV analysis was performed from 0 to 1.6 V potential window at various scan rates (5–100 mV/s). GCD analysis was tested at a current density from 0.3–8 A/g. The C_{sp}, specific energy (E) and specific power (P) of the ASC obtained from GCD curves were calculated according to Eqs (3–5):

$$C_{sp} = \frac{I \times \Delta t}{m \times \Delta V} \tag{3}$$

$$E = \frac{C_{sp} \Delta V^2}{2} \tag{4}$$

$$P = \frac{\Delta V I}{2m} \tag{5}$$

where C_{sp} (F/g) represents specific capacitance, Δt is discharge time (h), m (g) is the mass of active material (kg), ΔV (V) is the potential drop during the discharging time and I (A) is the applied current. EIS measurements were carried out in a frequency ranging from 0.01 Hz to 100 kHz at AC amplitude of 5 mV.

Received: 5 September 2019; Accepted: 30 October 2019;
Published online: 14 November 2019

References

1. Wang, J. G., Yang, Y., Huang, Z. H. & Kang, F. Coaxial carbon nanofibers/MnO_2 nanocomposites as freestanding electrodes for high-performance electrochemical capacitors. *Electrochimica Acta* **56**, 9240–9247, https://doi.org/10.1016/j.electacta.2011.07.140 (2011).
2. Cai, J. *et al*. High-performance supercapacitor electrode from cellulose-derived, inter-bonded carbon nanofibers. *Journal of Power Sources* **324**, 302–308, https://doi.org/10.1016/j.jpowsour.2016.05.070 (2016).
3. Xie, B. *et al*. Pseudocapacitive Co_9S_8/graphene electrode for high-rate hybrid supercapacitors. *Carbon* **141**, 134–142, https://doi.org/10.1016/j.carbon.2018.09.044 (2019).
4. Mohd Abdah, M. A. A., Abdul Rahman, N. & Sulaiman, Y. Enhancement of electrochemical performance based on symmetrical poly-(3,4-ethylenedioxythiophene) coated polyvinyl alcohol/graphene oxide/manganese oxide microfiber for supercapacitor. *Electrochimica Acta* **259**, 466–473, https://doi.org/10.1016/j.electacta.2017.11.005 (2018).
5. Mohd Abdah, M. A. A., Mohd Razali, N. S., Lim, P. T., Kulandaivalu, S. & Sulaiman, Y. One-step potentiostatic electrodeposition of polypyrrole/graphene oxide/multi-walled carbon nanotubes ternary nanocomposite for supercapacitor. *Materials Chemistry and Physics* **219**, 120–128, https://doi.org/10.1016/j.matchemphys.2018.08.018 (2018).
6. Li, Y. *et al*. Micro-/mesoporous carbon nanofibers embedded with ordered carbon for flexible supercapacitors. *Electrochimica Acta* **271**, 591–598, https://doi.org/10.1016/j.electacta.2018.03.199 (2018).
7. Lee, K. S., Park, C. W. & Kim, J.-D. Synthesis of ZnO/activated carbon with high surface area for supercapacitor electrodes. *Colloids and Surfaces A: Physicochemical and Engineering Aspects* **555**, 482–490, https://doi.org/10.1016/j.colsurfa.2018.06.077 (2018).
8. Chen, L. F., Lu, Y., Yu, L. & Lou, X. W. Designed formation of hollow particle-based nitrogen-doped carbon nanofibers for high-performance supercapacitors. *Energy and Environmental Science* **10**, 1777–1783, https://doi.org/10.1039/c7ee00488e (2017).
9. Mukhiya, T. *et al*. Engineering nanohaired 3D cobalt hydroxide wheels in electrospun carbon nanofibers for high-performance supercapacitors. *Chemical Engineering Journal* **361**, 1225–1234, https://doi.org/10.1016/j.cej.2019.01.006 (2019).
10. Zhou, Q., Wei, T., Yue, J., Sheng, L. & Fan, Z. Polyaniline nanofibers confined into graphene oxide architecture for high-performance supercapacitors. *Electrochimica Acta* **291**, 234–241, https://doi.org/10.1016/j.electacta.2018.08.104 (2018).
11. Mohd Abdah, M. A. A., Abdul Rahman, N. & Sulaiman, Y. Ternary functionalised carbon nanofiber/polypyrrole/manganese oxide as high specific energy electrode for supercapacitor. *Ceramics International* **45**, 8433–8439 (2019).
12. Mohd Abdah, M. A. A., Mohammed Modawe Aldris Edris, N., Kulandaivalu, S., Abdul Rahman, N. & Sulaiman, Y. Supercapacitor with superior electrochemical properties derived from symmetrical manganese oxide-carbon fiber coated with polypyrrole. *International Journal of Hydrogen Energy* **43**, 17328–17337, https://doi.org/10.1016/j.ijhydene.2018.07.093 (2018).
13. Zhu, Y., Shi, K. & Zhitomirsky, I. Polypyrrole coated carbon nanotubes for supercapacitor devices with enhanced electrochemical performance. *Journal of Power Sources* **268**, 233–239, https://doi.org/10.1016/j.jpowsour.2014.06.046 (2014).
14. Mohd Abdah, M. A. A., Zubair, N. A., Azman, N. H. N. & Sulaiman, Y. Fabrication of PEDOT coated PVA-GO nanofiber for supercapacitor. *Materials Chemistry and Physics* **192**, 161–169, https://doi.org/10.1016/j.matchemphys.2017.01.058 (2017).
15. Syed Zainol Abidin, S. N. J., Azman, N. H. N., Kulandaivalu, S. & Sulaiman, Y. Poly(3,4-ethylenedioxythiophene) doped with carbon materials for high-performance supercapacitor: A comparison study. *Journal of Nanomaterials* **2017**, 13, https://doi.org/10.1155/2017/5798614 (2017).
16. Zhang, K. *et al*. Poly(3,4-ethylenedioxythiophene) nanorods grown on graphene oxide sheets as electrochemical sensing platform for rutin. *Journal of Electroanalytical Chemistry* **739**, 66–72, https://doi.org/10.1016/j.jelechem.2014.12.013 (2015).
17. Xia, H. *et al*. Hierarchical heterostructures of Ag nanoparticles decorated MnO_2 nanowires as promising electrodes for supercapacitors. *Journal of Materials Chemistry A* **3**, 1216–1221, https://doi.org/10.1039/C4TA05568C (2015).
18. Canal-Rodríguez, M. *et al*. The role of conductive additives on the performance of hybrid carbon xerogels as electrodes in aqueous supercapacitors. *Electrochimica Acta* **295**, 693–702, https://doi.org/10.1016/j.electacta.2018.10.189 (2019).
19. Navarro-Pardo, F. *et al*. Effects on the Thermo-Mechanical and Crystallinity Properties of Nylon 6,6 Electrospun Fibres Reinforced with One Dimensional (1D) and Two Dimensional (2D) Carbon. *Materials (Basel)* **6**, 3494–3513, https://doi.org/10.3390/ma6083494 (2013).
20. Pech, O. & Maensiri, S. Electrochemical performances of electrospun carbon nanofibers, interconnected carbon nanofibers, and carbon-manganese oxide composite nanofibers. *Journal of Alloys and Compounds* **781**, 541–552, https://doi.org/10.1016/j.jallcom.2018.12.088 (2019).
21. Śliwak, A. & Gryglewicz, G. High-voltage asymmetric supercapacitors based on carbon and manganese oxide/oxidized carbon nanofiber composite electrodes. *Energy Technology* **2**, 819–824, https://doi.org/10.1002/ente.201402046 (2014).
22. Garcia-Torres, J. & Crean, C. Ternary composite solid-state flexible supercapacitor based on nanocarbons/manganese dioxide/PEDOT:PSS fibres. *Materials and Design* **155**, 194–202, https://doi.org/10.1016/j.matdes.2018.05.070 (2018).
23. Liang, Y., Wang, H., Sanchez Casalongue, H., Chen, Z. & Dai, H. TiO2 nanocrystals grown on graphene as advanced photocatalytic hybrid materials. *Nano Research* **3**, 701–705, https://doi.org/10.1007/s12274-010-0033-5 (2010).
24. Lee, T. H. *et al*. High energy density and enhanced stability of asymmetric supercapacitors with mesoporous MnO2@CNT and nanodot MoO3@CNT free-standing films. *Energy Storage. Materials* **12**, 223–231, https://doi.org/10.1016/j.ensm.2017.12.009 (2018).
25. Lindfors, T., Boeva, Z. & Latonen, R.-M. Electrochemical synthesis of poly(3,4-ethylenedioxythiophene) in aqueous dispersion of high porosity reduced graphene oxide. *RSC Advances* **4**, 25279, https://doi.org/10.1039/c4ra03423f (2014).
26. Sekhar, B. C., Babu, G. & Kalaiselvi, N. Nanoflake driven Mn_2O_3 microcubes modified with cooked rice derived carbon for improved electrochemical behavior. *RSC Advances* **5**, 4568–4577, https://doi.org/10.1039/C4RA11443D (2015).
27. Ogata, A., Komaba, S., Baddour-Hadjean, R., Pereira-Ramos, J. P. & Kumagai, N. Doping effects on structure and electrode performance of K-birnessite-type manganese dioxides for rechargeable lithium battery. *Electrochimica Acta* **53**, 3084–3093, https://doi.org/10.1016/j.electacta.2007.11.038 (2008).
28. Lai, C.-C. & Lo, C.-T. Preparation of Nanostructural Carbon Nanofibers and Their Electrochemical Performance for Supercapacitors. *Electrochimica Acta* **183**, 85–93, https://doi.org/10.1016/j.electacta.2015.02.143 (2015).
29. Ju, J. *et al*. Preparation and characterization of PVA-based carbon nanofibers with honeycomb-like porous structure via electro-blown spinning method. *Microporous and Mesoporous Materials* **239**, 416–425, https://doi.org/10.1016/j.micromeso.2016.10.024 (2017).
30. Sharaf El-Deen Sahar, E. A. *et al*. Evaluation of CNTs/MnO_2 composite for adsorption of 60Co(II), 65Zn(II) and Cd(II) ions from aqueous solutions. *Radiochimica Acta* **105**, 43, https://doi.org/10.1515/ract-2016-2624 (2017).
31. Zhang, L., Jamal, R., Zhao, Q., Wang, M. & Abdiryim, T. Preparation of PEDOT/GO, PEDOT/MnO_2, and PEDOT/GO/MnO_2 nanocomposites and their application in catalytic degradation of methylene blue. **10**, 148, https://doi.org/10.1186/s11671-015-0859-6 (2015).
32. Qi, B., Di, L., Xu, W. & Zhang, X. Dry plasma reduction to prepare a high performance Pd/C catalyst at atmospheric pressure for CO oxidation. *Journal of Materials Chemistry A* **2**, 11885–11890, https://doi.org/10.1039/C4TA02155J (2014).
33. Dong, P. *et al*. Highly enhanced photocatalytic activity of WO_3 thin films loaded with Pt–Ag bimetallic alloy nanoparticles. *RSC Advances* **7**, 947–956, https://doi.org/10.1039/C6RA25272A (2017).
34. Sidhu, N. K. & Rastogi, A. C. Bifacial carbon nanofoam-fibrous PEDOT composite supercapacitor in the 3-electrode configuration for electrical energy storage. *Synthetic Metals* **219**, 1–10, https://doi.org/10.1016/j.synthmet.2016.04.012 (2016).

35. Asen, P. & Shahrokhian, S. A High Performance Supercapacitor Based on Graphene/Polypyrrole/Cu_2O–$Cu(OH)_2$ Ternary Nanocomposite Coated on Nickel Foam. *The Journal of Physical Chemistry C* **121**, 6508–6519, https://doi.org/10.1021/acs.jpcc.7b00534 (2017).
36. Liu, Z. *et al*. Mesoporous carbon nanofibers with large cage-like pores activated by tin dioxide and their use in supercapacitor and catalyst support. *Carbon* **70**, 295–307, https://doi.org/10.1016/j.carbon.2014.01.011 (2014).
37. Gao, Y., Xia, Y., Wan, H., Xu, X. & Jiang, S. Enhanced cycle performance of hierarchical porous sphere $MnCo_2O_4$ for asymmetric supercapacitors. *Electrochimica Acta* **301**, 294–303, https://doi.org/10.1016/j.electacta.2019.01.173 (2019).
38. Xu, K., Li, S., Yang, J., Xu, H. & Hu, J. Hierarchical MnO_2 nanosheets on electrospun $NiCo_2O_4$ nanotubes as electrode materials for high rate capability and excellent cycling stability supercapacitors. *Journal of Alloys and Compounds* **678**, 120–125, https://doi.org/10.1016/j.jallcom.2016.03.255 (2016).
39. Syed Zainol Abidin, S. N. J., Mamat, M. S., Rasyid, S. A., Zainal, Z. & Sulaiman, Y. Electropolymerization of poly(3,4-ethylenedioxythiophene) onto polyvinyl alcohol-graphene quantum dot-cobalt oxide nanofiber composite for high-performance supercapacitor. *Electrochimica Acta* **261**, 548–556, https://doi.org/10.1016/j.electacta.2017.12.168 (2018).
40. Choudhury, A., Kim, J.-H., Yang, K.-S. & Yang, D.-J. Facile synthesis of self-standing binder-free vanadium pentoxide-carbon nanofiber composites for high-performance supercapacitors. *Electrochimica Acta* **213**, 400–407, https://doi.org/10.1016/j.electacta.2016.06.111 (2016).
41. Xu, J. *et al*. Facile synthesis of NiS anchored carbon nanofibers for high-performance supercapacitors. *Applied Surface Science* **434**, 112–119, https://doi.org/10.1016/j.apsusc.2017.09.233 (2018).
42. Lv, T. *et al*. Graphene oxide mediated self-sacrificial synthesis of $LaCO_3OH$-$Ni(OH)_2$@graphene hierarchical composite for photocatalytic H_2 evolution and supercapacitor. *Chemical Engineering Journal*, 123021, https://doi.org/10.1016/j.cej.2019.123021 (2019).
43. Nirmalesh Naveen, A. & Selladurai, S. Fabrication and performance evaluation of symmetrical supercapacitor based on manganese oxide nanorods–PANI composite. *Materials Science in Semiconductor Processing* **40**, 468–478, https://doi.org/10.1016/j.mssp.2015.07.025 (2015).
44. Lin, S.-C. *et al*. Asymmetric supercapacitors based on functional electrospun carbon nanofiber/manganese oxide electrodes with high power density and energy density. *Journal of Power Sources* **362**, 258–269, https://doi.org/10.1016/j.jpowsour.2017.07.052 (2017).
45. Syed Zainol Abidin, S. N. J., Mamat, S., Abdul Rasyid, S., Zainal, Z. & Sulaiman, Y. Fabrication of poly(vinyl alcohol)-graphene quantum dots coated with poly(3,4-ethylenedioxythiophene) for supercapacitor. *Journal of Polymer Science Part A: Polymer Chemistry* **56**, 50–58, https://doi.org/10.1002/pola.28859 (2018).
46. Wang, J.-G., Yang, Y., Huang, Z.-H. & Kang, F. A high-performance asymmetric supercapacitor based on carbon and carbon–MnO_2 nanofiber electrodes. *Carbon* **61**, 190–199, https://doi.org/10.1016/j.carbon.2013.04.084 (2013).
47. Kolathodi, M. S., Palei, M. & Natarajan, T. S. Electrospun NiO nanofibers as cathode materials for high performance asymmetric supercapacitors. *Journal of Materials Chemistry A* **3**, 7513–7522, https://doi.org/10.1039/C4TA07075E (2015).
48. Noh, J., Yoon, C.-M., Kim, Y. K. & Jang, J. High performance asymmetric supercapacitor twisted from carbon fiber/MnO_2 and carbon fiber/MoO_3. *Carbon* **116**, 470–478, https://doi.org/10.1016/j.carbon.2017.02.033 (2017).

Acknowledgements

The research leading to these results has received funding from the Universiti Putra Malaysia Research Grant (GP-IPS/2018/9619300).

Author contributions

Y.S. supervised and coordinated the whole experiments, M.A.A.M.A. conducted the experiment(s), analysed the results and wrote the main manuscript. N.H.N.A. and S.K. wrote the manuscript. All authors reviewed the manuscript.

Competing interests

The authors declare no competing interests.

Additional information

Correspondence and requests for materials should be addressed to Y.S.

Reprints and permissions information is available at www.nature.com/reprints.

Publisher's note Springer Nature remains neutral with regard to jurisdictional claims in published maps and institutional affiliations.